AGU PUBLICATIONS

Water Resources Research

RESEARCH ARTICLE
10.1002/2016WR019726

A new geophone device for understanding environmental impacts caused by gravel bedload during artificial floods

Ryota Tsubaki[1], Yoshihisa Kawahara[2], Xin-Hua Zhang[3], and Kentaro Tsuboshita[4]

[1]Department of Civil Engineering, Nagoya University, Furo-cho, Chikusa-Ku, Nagoya, Japan, [2]Department of Civil and Environmental Engineering, Hiroshima University, 1-4-1 Kagamiyama, Higashi-Hiroshima, Japan, [3]State Key Laboratory of Hydraulics and Mountain River Engineering, Sichuan University, Chengdu, China, [4]Taisei Corporation, 1-25-1 Nishi-shinjuku, Shinjuku, Tokyo, Japan

Key Points:
- We developed a geophone device and established empirical models for estimating the size of grains impinged onto the device
- We installed a number of geophone devices in a cobble-bed river and analyzed gravel transport during artificial floods
- In the text, we discuss our results and the consequences of gravel bedload on the removal of attached-algae and aquatic plants

Correspondence to:
R. Tsubaki,
rtsubaki@civil.nagoya-u.ac.jp

Citation:
Tsubaki, R., Y. Kawahara, X.-H. Zhang, and K. Tsuboshita (2017), A new geophone device for understanding environmental impacts caused by gravel bedload during artificial floods, *Water Resour. Res.*, *53*, 1491–1508, doi:10.1002/2016WR019726.

Received 31 AUG 2016
Accepted 17 JAN 2017
Accepted article online 24 JAN 2017
Published online 15 FEB 2017

Abstract To assess the contribution of gravel bedload on the removal of attached-algae and aquatic plants from a cobble-bed river during small floods, we propose a geophone type method for measuring the local bedload of non-uniform sized gravel. Due to limited peak discharge for focused events during our study, a large fraction of bed material (here cobbles) was immobile and only a small fraction of bed material (sand and gravel) was expected to be transported during the flushing flows we analyzed. The device we developed has a size equivalent to immobile bed material and a shape similar to bed material (rounded cobbles) at the site. The instrument's design allows avoidance of disturbances in river bed micro-topography during installation and local bedload transport during floods. A flume experiment was conducted in order to establish an empirical algorithm for estimating the diameter of impacted gravel, and uncertainty related to diameter estimation is discussed. The proposed method was utilized to quantify gravel bedload in a cobble-bed river during flushing flows. We also discuss the contribution of measured gravel bedload during flushing flows on the removal of attached-algae (up to a 37% reduction in chlorophyll-a density) and aquatic plants (a reduction of 38% in dry mass per area). Based on time variation for the measured gravel bedload, we also suggest the propagation of a bed-form composed of the fine sediment fraction migrating on immobile larger sediment and implications for the propagation of the fine sediment wave for attached-algae removal.

1. Introduction

1.1. Ecosystem and Sediment Transport

Sediment transport during floods regulates topography along the alluvial stream. Sediment transport also regulates aquatic ecology [e.g., *Pitlick and Wilcock*, 2001]. Such regulation is prominent in mountainous streams paved with gravel and cobbles that have been transported during floods following precipitation and snowmelt events. In gravel/cobble-bed rivers, periphyton (attached-algae) and macrophytes (aquatic plants) are the main primary producers within the aquatic ecological environment. Attached-algae and aquatic plants grow during normal flow periods and are removed from river beds during floods due to the strong flow accompanied by sediment transport (Figure 1) [*Horner et al*., 1990; *Peterson*, 1996; *Wolfert et al*., 2001; *Jones et al*., 2012]. Some species utilize flood event disturbances for downstream migration. The detachment of aged algae and the removal of old branches of aquatic plants may activate the growth of these species following disturbances. Accordingly, flood flow and sediment transport have strong and multilateral impacts on mountainous river ecosystems.

1.2. Difficulty in Numerical Assessments of the Non-Uniform Sediment Transport Rate in Steep-Sloped Rivers

Non-uniform sized sediment transport in gravel/cobble-bed rivers is complex [*Clayton and Pitlick*, 2007]. Over the years, various numerical models have been proposed and used for assessing sediment transport in gravel/cobble rivers [*Parker*, 2008] but, in practice, accuracy is still limited [*Tsakiris et al*., 2014].

One reason sediment transport models have limited accuracy is related to the high inhomogeneity of bed-material size for both the horizontal and vertical directions of mountainous rivers [*Gibson et al*., 2009]. Due to grain sorting processes, the river-beds of mild-slope rivers consist of relatively uniform sand

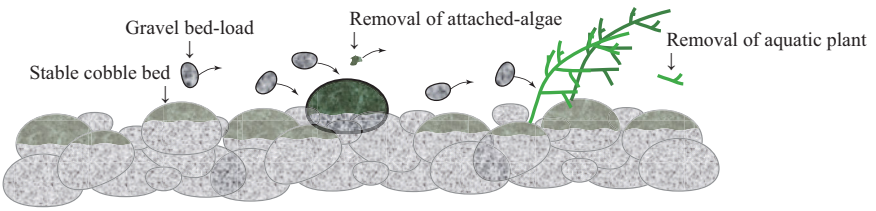

Figure 1. A schematic of the removal of attached-algae and aquatic plants due to bedload during a flood.

[*Parker*, 1991]. On the other hand, the bed of mountainous rivers is composed of a wide range of bed-materials including sand (less than 2 mm in diameter), boulders (larger than 256 mm in diameter), and intermediate diameter sediment classes [*Clayton and Pitlick*, 2007]. Thus, preparing a three-dimensional representation of grain-size distributions is a challenging task, especially when the resolution and accuracy of available grain size data are generally limited.

Flow within steep-sloped rivers is complex for both high and normal flow conditions [e.g., *Clifford et al*., 1992; *Shvidchenko and Pender*, 2001; *Powell*, 2014]. The complexities associated with both sediment transport and flow make estimating sediment transport processes in gravel/cobble-bed rivers challenging from both an engineering and scientific viewpoint [*Yager et al*., 2007]. Therefore, the calibration and validation of sediment transport models are indispensable for obtaining quantitative estimations [*Tsakiris et al*., 2014].

1.3. Three Approaches for Sediment Transport Quantification

Evaluations of sediment transport amounts as determined from numerical models have stringent accuracy limitations, especially in rivers with non-uniform bed material. For this reason, direct measurements of sediment transport in streams are quite useful and essential for estimating sediment transport amounts, for calibrating/validating sediment transport models, and for assessing the ecological impacts of sediment transport during floods.

Sediment transport measurements can be categorized as either: (1) direct sampling, (2) indirect sampling, or (3) inverse estimations based on morphological change analyses [*Diplas et al*., 2008; *Raven et al*., 2010]. Direct sampling methods sample moving sediment using instruments equipped with containers. Sediment caught in containers is quantified and a sediment flux is calculated. Due to the complexity of transport phenomena including armoring [e.g., *Shen and Lu*, 1983], the organization and propagation of bed-forms [e.g., *Kleinhans et al*., 2002], and varying flow conditions, bedload transport in gravel/cobble-bed rivers is highly episodic. Such complexities require the high spatial and temporal resolution of bedload measurements, leading to impractical demands in regards to the labor and resources required to achieve direct sampling for sediment transport in gravel/cobble-bed rivers during floods.

Indirect sampling utilizes acoustic/ultrasonic sound [*Mizuyama et al*., 2003; *Uchida et al*., 2013], impact counters [*Rickenmann and McArdell*, 2007; *Reid et al*., 2007; *Raven et al*., 2010], or electromagnetic pulses [*Chung and Lin*, 2011] for evaluating sediment transport amounts. Acoustic approaches employ a device that is referred to as a hydrophone and the recorded sound wave is correlated to the amount of sediment transport. Impact counters detect the occurrence of sediment impingement on the device. In general, the grain-size distribution of sediment flux is separately estimated using acoustic/ultrasonic and impact counting approaches [e.g., *Rickenmann et al*., 2012]. Indirect approaches have an advantage in that they allow continuous measurements with relatively inexpensive operation costs [*Tsakiris et al*., 2014]. To conduct continuous measurements, a geophone sensor with a cover/protection plate must be rigidly fixed in the cross section of the stream in order to prevent wash-out or the deformation of devices. Accordingly, geophone devices have been installed in rigid structures such as weirs and dams [*Mizuyama et al*., 2003; *Rickenmann and McArdell*, 2007; *Mizuyama et al*., 2010; *Rickenmann et al*., 2012; *Tsakiris et al*., 2014]. A device for storing and processing signals is generally separate and is placed on the side of a stream in order to achieve accessibility to measured data and to secure enough space for devices, including batteries and data transmitters. The utilization of electromagnetic pulses has also been successfully applied for measuring high concentrations of suspended-sediment flux [*Chung and Lin*, 2011]. Turbidity measurements are also widely used for

estimating suspended sediment concentrations but these approaches are not applicable for measuring gravel bedload amounts.

A third approach focuses on the relationship between local sediment transport and evolution of the macroscopic/mesoscopic morphology of stream beds. Repeated topography surveys are needed for this approach so changes in morphology can be followed [*Raven et al*., 2010]. In practice, the utilization of a multibeam depth sounder has become a popular tool for measuring high-resolution river bed topography [*Vericat et al*., 2014; *Muste et al*., 2016]. This type of high-resolution measurement enables researchers to follow ripple/dune migration and makes it possible to estimate sediment budgets based on such microscopic morphology changes. The morphological sediment budget approach presumes that bed-form changes are observable and that the grain-size is uniform (or at least that the grain-size distribution is constant). The approach is not suitable for measuring partial gravel transport in cobble-bed rivers during small floods because bed morphology does not change during floods.

1.4. Objectives of This Study

In this study, a method for measuring local, unsteady, non-uniform gravel transport in cobble-bed rivers was developed in order to reveal the gravel transport process during small floods when only the smaller fraction of bed-material is subject to transport. Such selective sediment transport is common in gravel-bed rivers with moderate to small flood disturbances [*Lisle*, 1995; *Kuhnle et al*., 2006; *Yager et al*., 2007; *Parker*, 2008; *Tuijnder et al*., 2009].

The method we developed was used to investigate local gravel transport during flushing flows. The quantity of attached-algae and aquatic plants located near areas of sediment transport measurements were surveyed prior to and following the implementation of flushing flows. Below, we discuss the impact of sediment transport during flushing flows on attached-algae [*Horner et al*., 1990; *Tsujimoto and Tashiro*, 2004; *Fovet et al*., 2012] and aquatic plant [*Jones et al*., 2012] removal from the bed. Evidence of sand/gravel, bed-form migration on the coarser immobile bed was observed by analyzing the obtained data; its implication to attached-algae removal is also discussed.

The principal behind the method we developed is the same principle that is currently used for hydrophones [e.g., *Mizuyama et al*., 2003; *Oda et al*., 2011; *Hasegawa and Miyamoto*, 2014] or geophones [e.g., *Rickenmann and McArdell*, 2007]. The exception to the current hydrophone/geophone approach in relation to our method is that we focused on measuring local sediment transport in an actual river bed during a relatively small flood. Therefore, the procedure we propose is less disruptive to bed topography as compared to classical geophone applications that require a rigid cross section for positioning the measurement system during large flood events [e.g., *Uchida et al*., 2013; *Tsakiris et al*., 2014]. Due to relatively limited amounts of bedload and the small size of our device, we were able to analyze the individual impact of sediment particles (similar to the impact counter approach). The device we developed consists of consumer products, including a sound recorder. As a result, the device is inexpensive and a number of devices can be distributed within a river-bed for the purpose of understanding the spatial inhomogeneity of sediment transport.

1.5. Paper Organization

In section 2, we describe the method we developed for measuring gravel transport. A flume experiment was conducted in order to establish a relationship between impact acoustic waveforms and the size of impacting sediment. The results of this experiment are reported in section 3. Descriptions regarding the field site and target events are summarized in section 4. In section 5, we present results obtained during flushing flows conducted from March 2013 to March 2014, as well as results obtained for sediment transport and its relationship to attached-algae detachment and aquatic plant removal. Concluding remarks are provided in section 6.

2. Methods

2.1. The Device

A schematic of the measuring device is provided in Figure 2. The unit consists of (1) a steel shell that is 240 mm in diameter and 1 mm in thickness, (2) a digital sound recorder, and (3) a 20 kg iron weight. The steel shell was loosely mounted on an iron weight using a foamed rubber sheet and plastic banding to dampen the Eigen frequency vibration of the steel shell. Air within the steel shell was exhausted when the

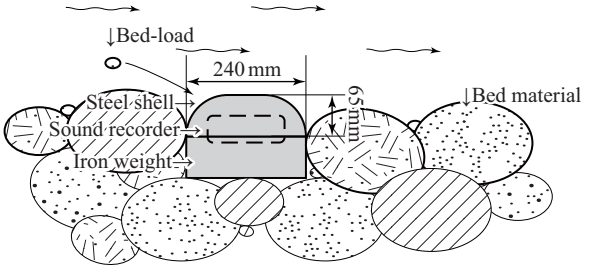

Figure 2. A schematic of the measuring device in a stream.

device was installed within the river bed. The impact of sediment saltation on the steel shell created an acoustic wave that was recorded by the digital recorder housed inside the steel shell. We employed two models of sound recorder: (1) the RR-XS450 manufactured by the Panasonic Co. and (2) the Zoom H4n manufactured by the Zoom Co. The RR-XS450 has smaller dimensions (41 mm × 103 mm × 16 mm) and its highest recordable frequency is 44.1 kHz. The Zoom H4n has a larger body size (73 mm × 156 mm × 35 mm) and is capable of recording sound waves at 96 kHz. To prevent water immersion into the recorder, we covered the sound recorder with plastic bags. Figure 3 displays a series of photos for actual device installation within the river bed. Since we expected sediment impacts to be biased toward the upstream side of the device, sound recorder microphones were directed in the upstream direction in order to efficiently capture the sound of sediment impacts.

2.2. Acoustic Waves

Figure 4 provides an example of an acoustic waveform recorded by the digital recorder housed in the steel shell during a flushing flow. The fluctuation of sound pressure increased after the water level increased, beginning at 10:30 (Figures 4a and 4b). Fluctuations in sound pressure consist of: (1) sediment impact sounds, (2) the characteristic vibration of the steel shell, and (3) pressure fluctuations due to flow turbulence. Sediment impacts have a substantially higher frequency, 3.5–10 kHz in this study, as compared to characteristic vibrations and turbulent fluctuations having an order of 10–100 Hz (Figure 4d). To extract sediment impact sounds (Figures 4c, 4e, and 4f), we applied a high-pass filter of 1 kHz to the raw data (Figures 4b and 4d). Sound pressure in this study was non-dimensional because commercial sound recorders were used.

The sound impulse sequence consists of (a) an impact phase, (b) a transition to the characteristic frequency of the steel shell, and (c) the attenuation phase. For the purpose of this study, the features of the impact phase were reduced to the following: P_{max}, a maximum sound pressure; T_{imp}, the impact duration; and $T_{1/10}$, the duration required to reduce the pressure fluctuation below 10% of maximum pressure (Figure 4f). *Goto et al*. [2014] reported that the pipe hydrophone has a dominant frequency of 4 kHz, corresponding to the Eigen frequency of the pipe used in their experiment. Our system was designed not to obtain the Eigen frequency but the initial waveform of impact.

2.3. Attached Algae Density and Aquatic Plant Biomass Prior To and Following Flushing Flows

To evaluate the reduction of attached-algae and aquatic plants surrounding sediment measurement points, biofilm attached to cobbles was collected from a 0.05 m by 0.05 m sampling area and plant bodies were

Figure 3. Photos of the installation of a device in the river bed.

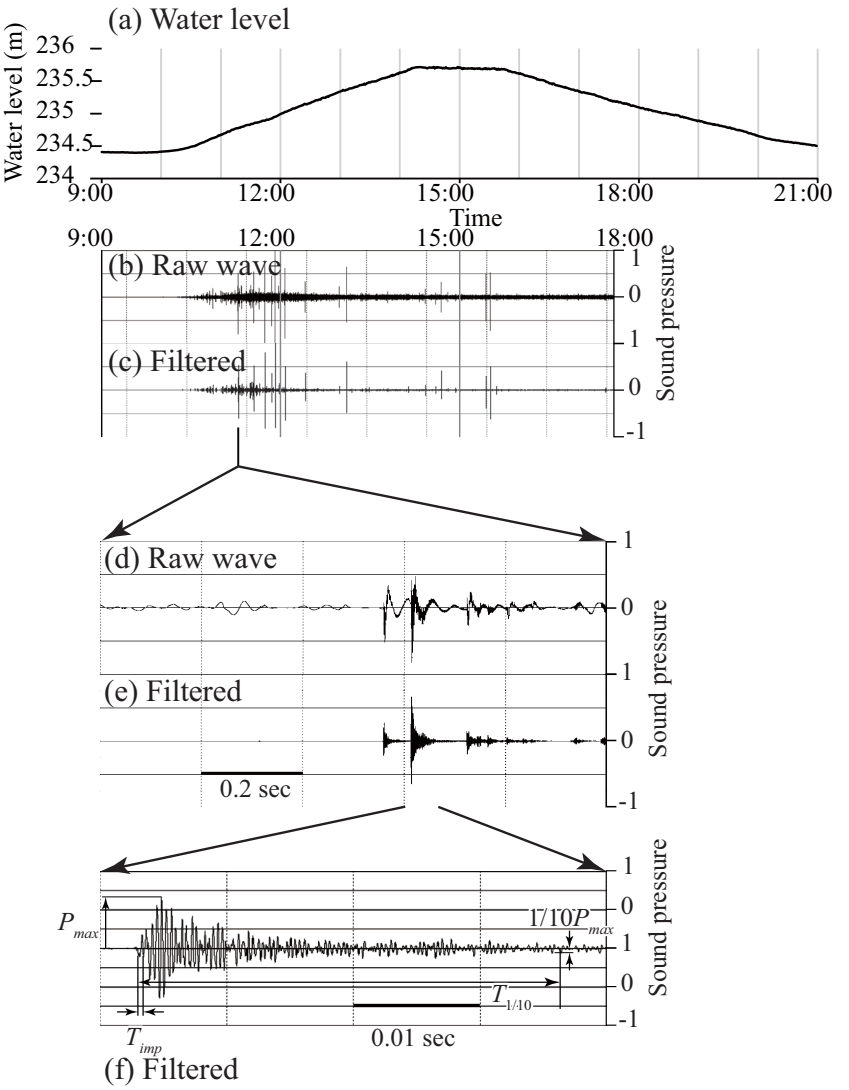

Figure 4. An example of an acoustic waveform with a local water level time-series. (a) A time-series for the local water level; (b) a recorded raw acoustic wave profile; (c) a sound wave after applying a 1 kHz high-pass filter; (d) a close up of the raw sound wave; (e) a close up of the filtered sound wave; and (f) a close up of an impact sound and the definition of P_{max}, T_{imp}, and $T_{1/10}$.

collected from a 0.3 m by 0.3 m sampling area. Chlorophyll-a (chl-a) concentrations included in the biofilm of each sample were evaluated based on the absorption spectroscopy of an 80% aqueous acetone buffered solution [*Porra et al*., 1989]. Three cobbles were sampled at each sample point, and an average and standard deviation of chl-a density for each sample point were calculated. For aquatic plant biomass, sampled plant bodies were dried at 110°C for up to 48 h, a dried mass per area (dry g/m^2) was obtained [*Miura et al*., 1976; *Feijoó et al*., 1996], and the mean of dry weight per unit area from four samples was calculated.

3. Calibration of a Bedload Estimation Model and the Correction of Bias in Estimates

3.1. Experimental Conditions

To calibrate a model for estimating the mass of each impinging sediment particle from the sound wave profile, a series of particle impact experiments was conducted using an experimental channel. As summarized in Table 1, glass spheres and river gravel were the materials employed as impacting particles. Three size classes of glass spheres were used. In the text, the three groups are referred to as S12, S20, and S30, and correspond to diameters of 12 mm, 20 mm, and 30 mm, respectively. Hereafter, the term *size class* is used

Table 1. Particle Groups Used During the Sediment Impact Experiment

Group Name	Material	Diameter Size Class (mm)	Mean Mass (g)
S12	Glass sphere	12	2.5
S20		20	9.9
S30		30	36
G08	Sieved river gravel	6.7–10 (sieve size)	0.92 (44.1 kHz)/ 1.17 (96 kHz)
G13		10–15 (sieve size)	2.2/2.4
G20		15–25 (sieve size)	7.3/5.72
G28		25–30 (sieve size)	15.7/16.1

to specify the grain size and the term *group* is used to specify both the material and the size class. Four size classes of sieved river gravels were prepared. In the text, the four groups are referred to as G08, G13, G20, and G28, and correspond to the sieve opening sizes indicated in Table 1. The amplitude of the impact sound is proportional to the mass and the impact velocity of an impinging particle. Acoustic waveforms caused by impacting particles that are too small are difficult to distinguish in relation to environmental and system noise. For this study, we focused on detecting the impact of grains larger than 6.7 mm in diameter. During the experiment, 50 particles of each particle group were released 0.3 m upstream from the measuring device. The mean mass of particles for each size class is summarized in Table 1. Two sound recorders were used: (1) a RR-XS450 distributed by the Panasonic Co. that is capable of recording sound waves at 44.1 kHz and (2) a Zoom H4n distributed by the Zoom Co. that is capable of recording at 96 kHz. The mean mass of sieved river gravel differed each time gravel was sieved because each group only consisted of 50 particles and the shape and grain-size distribution of river gravel prior to sieving was not perfectly constant. The mean mass obtained for experiments conducted using the 44.1 kHz recording and the 96 kHz recording are provided in Table 1.

Figure 5 provides plane- and side-views of the experimental channel. Cobbles of approximately 50 mm in diameter were fixed in a staggered arrangement on the channel bed in order to model roughness at the field site. Table 2 displays the two flow cases used during the calibration experiment. Bed shear stress and the Manning's coefficient in Table 2 were estimated based on channel slope, water depth, and flow rate. The range of mean bed shear stress was designed for representing peak bed shear stress at the field site during the flushing flow event described in section 4.3.

3.2. Number of Impact Counts

The measurement device employed counts a number of sediment impacts. The shape of the measurement device mimics the form of bed material. For estimating the contribution of sediment impacts on attached-algae removal, determining the actual number of impacts to bed material is essential rather than determining the number of sediment particles transported on the bed. To understand the sediment rate of bedload per unit width from the measured results, bias related to impact count, as discussed below, must be understood.

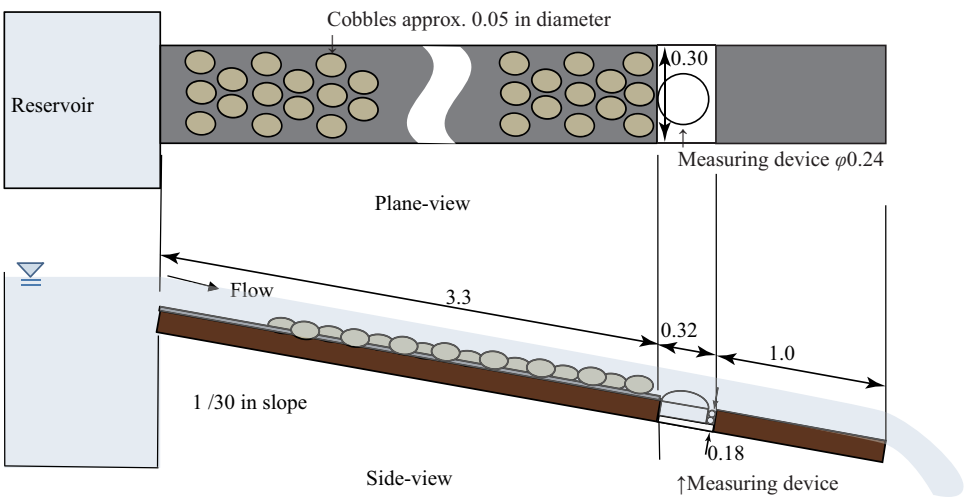

Figure 5. Schema of an experimental channel (not to scale, dimensions in m).

Table 2. The Flow Case List for the Calibration Experiment

Case Name	Flow Rate	Water Depth	Channel Slope	Bed Shear Stress	Channel Width	Mean Velocity	Froude Number	Manning's Coefficient
Q30	0.030	0.11	0.033	36	0.30	0.91	0.88	0.046
Q20	0.020	0.095	0.033	31	0.30	0.70	0.73	0.054

If a particle overpasses the device without making contact, information related to the overpassed particle cannot be detected by the device. Such an outcome is the first type of bias in impact counts. In the event that a particle contacts the device twice, the recorded number of impacts will be greater than the actual number of particles passing. Such an outcome is the second type of bias. Figure 6 displays an example of an acoustic wave that occurs due to a double impact by a single particle. Figure 7 provides the relationship between particle diameter, total impact count, and no contact occurrence per a 50 particle release. Results obtained for the two recording frequencies (44.1 and 96 kHz), the two types of particle materials (glass spheres and river gravel), the different grain-size classes, and the two flow conditions (Q30 and Q20) are plotted in Figure 7. The distribution of total impact (filled circles) and no contact (open circles) has dispersion, but the total impact increases with diameter and the *no contact* number approaches zero for larger diameters. The sensitivity of the grain diameter to the detection rate was also reported in *Mizuyama et al.* [2010].

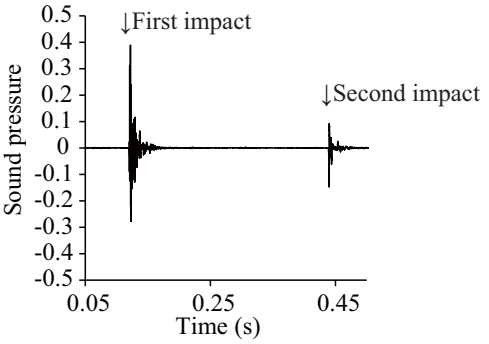

Figure 6. An example of an acoustic wave containing two impacts by a single particle.

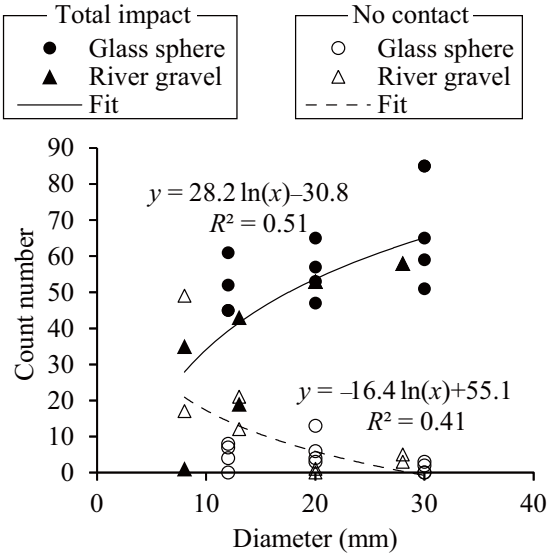

Figure 7. The relationship between particle diameter, total impact count, and no contact occurrence per 50 particles released.

Regression curves for total impact and no contact are plotted in Figure 7. The established determination coefficients were $R^2 = 0.51$ and 0.41 for total impact and no contact, respectively. The fitting curve for the no contact (dashed line) plot indicates that approximately 20% (10 out of 50 particles) of the 20 mm diameter particles passed without contact to the device. The count number for this diameter class was approximately 50. The result implies that for the 20 mm diameter class, 20% of particles passed without contact and the remaining 80% of particles came in contact, 25% more than the actual number of particles. For the 30 mm diameter class, almost all of the particles contacted the device and the total impact number was overestimated by approximately 20%. For the 10 mm diameter class, 40% of particles overpassed the device and 40% were underestimated in the total count number as compared to the actual number of particles released.

On a uniform grain bed, the height and step length of particle saltation were reported as 1–100 times the particle diameter and increased with the increase of total bed shear stress [*Sekine and Kikkawa*, 1992; *Niño et al.*, 1994]. In this study, the scale of bed roughness and the dimensions of the measuring device were larger than the moving particle diameters. Here, it is worth noting that the trajectory of saltation may be regulated not only by the size of saltation gravel but also by the scale of bed roughness [*Papanicolaou et al.*, 2001]. Accordingly, the relationship found in Figure 7 depends on bed roughness and flow situations.

3.3. Estimation of the Mass of Impacting Particles

Based on physical impact theories of a sphere on a flat plate [*Zener*, 1941; *Love*, 1944: *Igarashi et al.*, 1984], the impact force, F, is:

$$F = \alpha m^{2/3} v^{6/5} \quad (1)$$

where α is a physical constant, m is the mass of the impact particle, and v is the impact velocity. The impact duration, T_{imp}, is:

$$T_{imp} = \beta m^{1/3} v^{-1/5} \quad (2)$$

where β is a physical constant. *Igarashi et al.* [1984] conducted an impact experiment in the air and verified a linear relationship between the impact force, F, and the peak sound pressure, P_{max}. Based on this relationship, F can be replaced by P_{max} and the mass, m, can be estimated based on equations (1) and (2) using an exponential function:

$$m = \gamma {P_{\max}}^{3/8} {T_{imp}}^{9/4}. \quad (3)$$

where γ is a physical constant. For this study, we used a rounded steel shell as the impact plate and submerged the device in the water. In impact theory (equations (2) and (3)), T_{imp} is the duration of plate deformation. For the purpose of this study, T_{imp} represents the wave duration for sound propagated inside the steel shell during the impact phase. Depending on the conditions for equation (3), the outcomes of these types of situations considerably differ. Equation (3) expresses the significance of wave duration for the impact phase T_{imp} as well as for P_{max}. In our submerged experiment for particle impacts, the variability of T_{imp} for a constant impact condition was quite large as compared to the preliminary experiment conducted in air. A large variability for T_{imp} during the submerged measurement was expected given the complexity of sound wave propagation within the rounded shell filled with water. We also introduced another input parameter, $T_{1/10}$, into the mass estimation equation. The parameter $T_{1/10}$ represents the duration required to reduce the pressure fluctuation below 10% of maximum pressure. The parameter $T_{1/10}$ is related to the decay property of shell vibration and to the efficiency of high frequency fluctuation modulations at the impact phase due to lower frequency fluctuations during the attenuation phase. Therefore, $T_{1/10}$ is expected to be affected by wave frequency during the impact phase.

The empirical equations for the 44.1 kHz and 96 kHz recorders, as required for estimating particle mass from acoustic waveforms that minimize deviations from the actual mean of particles as obtained from the corresponding experimental cases, were identified as:

$$m = 17.3 \times 10^3 {P_{\max}}^{1.38} {T_{imp}}^{0.280} {T_{1/10}}^{0.546} \quad (4)$$

for the 44.1 kHz recording and:

$$m = 14.6 \times 10^3 {P_{\max}}^{1.38} {T_{imp}}^{0.280} {T_{1/10}}^{0.546} \quad (5)$$

for the 96 kHz recording. Here, m is the estimated mass of the particle in grams, P_{max} is the peak pressure amplitude (non-dimensional), T_{imp} is the duration of the first two waves during the impact phase in milliseconds, and $T_{1/10}$ is the duration required to reduce the amplitude to $1/10 P_{max}$ in a second. The schematic definitions of P_{max}, T_{imp}, and $T_{1/10}$ are provided in Figure 4f.

Figure 8 compares the mean mass of released particles and the mean mass estimated from acoustic waveforms using equations (4) and (5). Each of the plotted points corresponds to a mean of 50 particles released. Using the empirical equations, we were able to estimate the mass of impacting particles as a mean. For the estimation, better agreement was determined using 44.1 kHz and deviation from the 1:1 line was almost within $\pm$20%; whereas deviation from the 1:1 line for the 96 kHz recorder was approximately 40% with the exception of one outlier.

The coefficients in equations (4) and (5) were determined to best fit the mean of the actual and estimated particle masses for each experimental case. Particle-wise estimations displayed much more uncertainty as compared to their means. The distributions of the estimated masses for each of the 96 kHz experimental cases are provided in Figure 9. The standard deviation for each experimental case was close to the corresponding mean (see Table A1). Based on the large standard deviations, approximately 100 impact events of uniform sized grains were required in order to obtain the mean of grain sized particles with a 10% standard error. Even the error for mass estimations for each event was considerably large. The statistical significance was $p < 0.001$ for the correlation between the estimated and actual mass for the two datasets recorded at

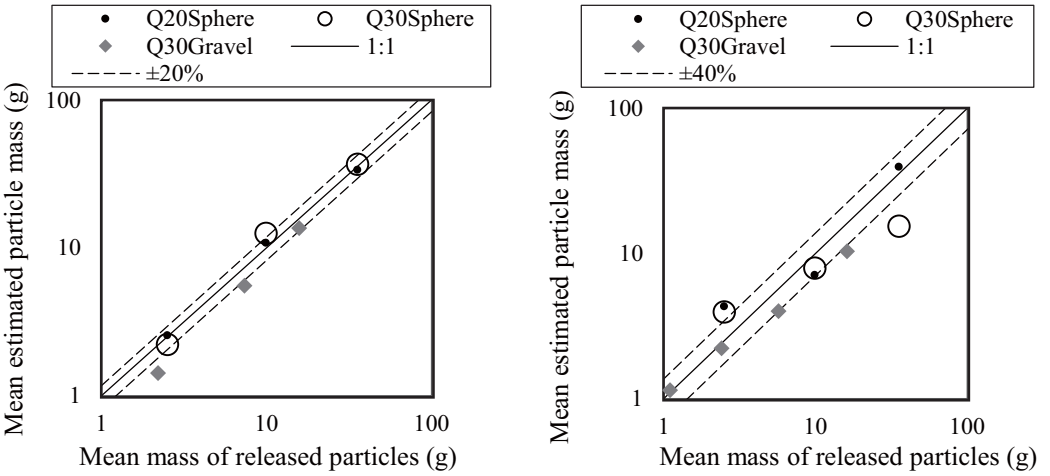

Figure 8. The actual mean mass and the estimated mean mass of particle groups for the different size classes and materials; and the flow cases for the 44.1 kHz (left) and 96 kHz (right) recorders.

44.1 kHz and 96 kHz. Therefore, the method developed in this study is theoretically useful for estimating trends in impact particle mass if a substantial number of impacts are analyzed.

In section 3.2, we discussed the case of multiple impacts for a single particle. The mass estimation displayed in Figures 8 and 9 only dealt with the initial impact for multiple impacts. Figure 10 summarizes the mean mass for second impacts, evaluated using the model parameterized using first impact data. The estimated mass for second impacts underestimated actual grain mass by 61%. The result indicates that the mean for estimated mass tends to be underestimated in proportion to the number of multiple impact occurrences and that a correction is required for cases where the occurrence of multiple impacts is non-negligible.

3.4. Correction of the Grain-Size Distribution and the Impact Count Obtained From Field Data

To analyze bedload trends from field data, grain-size was divided into four classes: 6.7–10 mm (d_{g1}), 10–15 mm (d_{g2}), 15–22.5 mm (d_{g3}), and 22.5–33.8 mm (d_{g4}). The ratio between neighboring grain-size classes was 1.5. In section 3.3, the mass of particles was used as a grain-size indicator because mass is a better indicator for describing sediment impact on a plate rather than diameter. However, in river engineering, grain size is customarily and frequently classified by diameter (or sieve opening length) rather than grain mass. Therefore, the mass of particles estimated from an acoustic waveform (m) is converted to an equivalent sphere diameter (d) by:

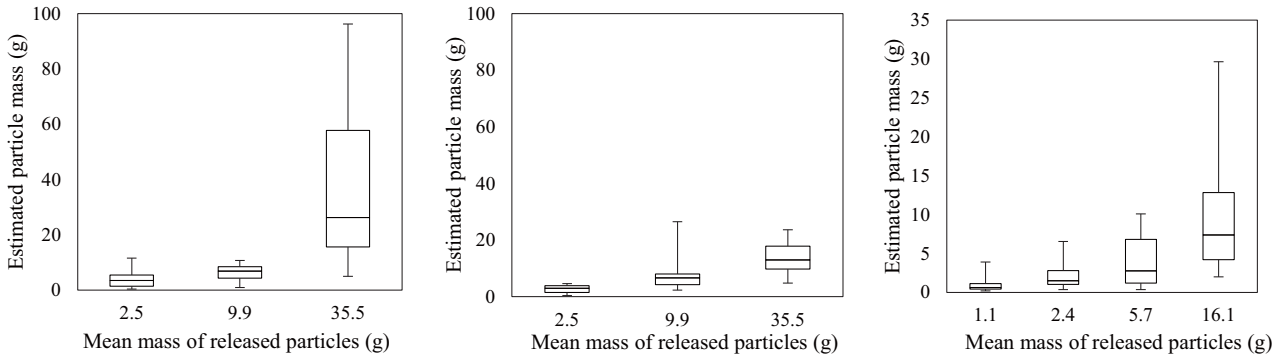

Figure 9. The distribution of estimated particle masses for each experimental case (the result of Q20/glass spheres on the left, Q30/glass spheres in the center, and Q30/river gravel on the right). The top and bottom bars statistically correspond to 5% and 95%, respectively; the top and bottom of boxes correspond to 25% and 75%, respectively; and the band inside the box indicates 50% based on the release of 50 particles.

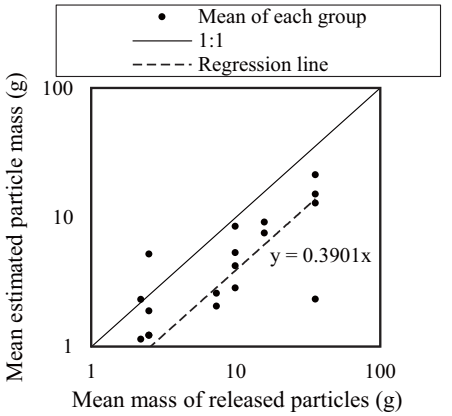

Figure 10. The actual mean mass and the mean estimated mass for the second impact for multiple impacts.

$$d = 2\left(m\frac{3}{4\pi\rho_s}\right)^{1/3}, \tag{6}$$

while assuming a sediment density of $\rho_s = 2650$ kg/m^3. The probability distribution of the correct diameter ($d_{correct}$) divided by the estimated diameter ($d_{estimated}$) for 681 impact events was calculated and is provided in Figure 11a. The distribution reveals the probability distribution of actual grain size based on estimated grain size. Even if the size of the bed material is perfectly uniform, the estimated grain-size distribution is dispersed due to this error. Conversely, a more likely grain-size distribution can be determined by accounting for grain-size dispersion errors in estimations by adopting the inverse problem concept [*Yeh*, 1986]. The class of grain size is divided by the ratio of 1.5, and the probability density for each grain class is depicted in Figure 11b. The probability density of the grain-size is denoted as $D_{p,-2}$, $D_{p,-1}$, $D_{p,0}$, and $D_{p,1}$ for the relative grain-classes of 0.36–0.54, 0.54–0.82, 0.82–1.22, and 1.22–1.84 (as shown in Figure 11b). For our assessment, we assumed that the measured grain-size distribution (d_{g1}, d_{g2}, d_{g3}, and d_{g4}) was the initial value of the probable grain-size distribution ($d_{gx,i}$: $x = 1$, 2, 3, and 4). The convolution of the probable grain-size distribution and the grain-size error can be calculated using:

$$d_{gx,n} = \sum_{j=-2}^{1} D_{p,j}\, d_{gx-j,i}. \tag{7}$$

Calculating $d_{g1,n}$ in equation (7) requires the grain-size distribution of the smaller class, $d_{g0,i}$. However, due to low signal/noise ratio, d_{g0} (as an initial value of $d_{g0,i}$) cannot be estimated from the measurement. As a result, we assumed $d_{g0,i} = d_{g1}$ for the initial value. After all of the $d_{gx,n}$s were calculated, the sum of the square error between the observed d_{gx} and the estimated $d_{gx,n}$ was calculated based on:

$$\mathrm{Err} = \sum_{x=1}^{3} (d_{gx} - d_{gx,n})^2. \tag{8}$$

The initial grain-size distribution, $d_{gx,i}$, was modified in order to minimize the error defined in equation (8). The grain-size distribution providing the least square error was the probable grain-size distribution for non-uniform field data.

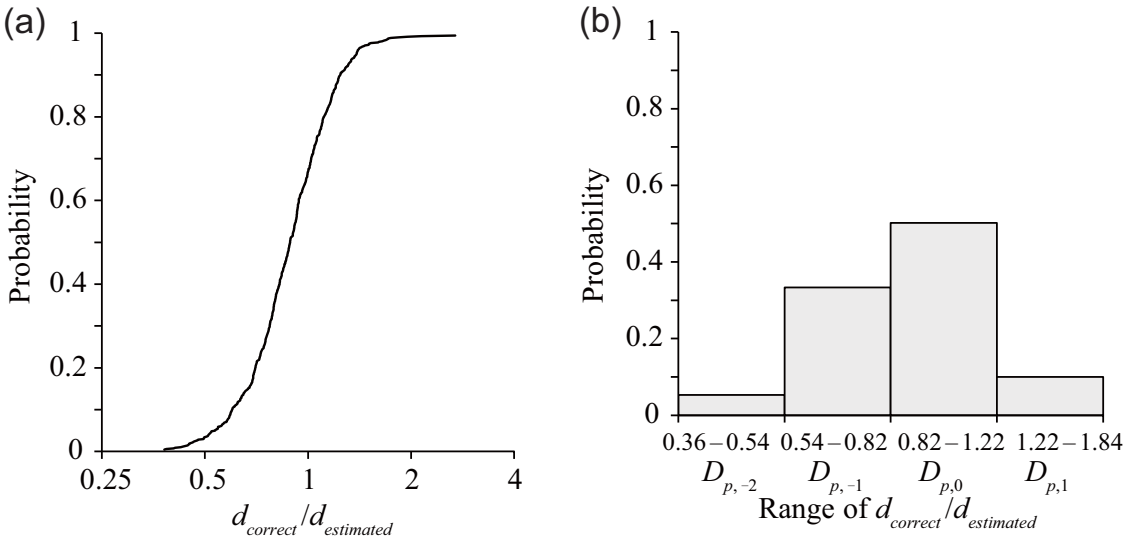

Figure 11. The probability curve (left: a) and the histogram (right: b) of the $d_{correct}/d_{estimated}$ distribution based on the flume experiment.

To assess bedload amounts, underestimation of sediment counts due to no contact can be corrected for each grain-size class using the regression line provided in Figure 9, namely:

$$n_{corrected} = n_{raw}(-16.41\ln(d) + 55.052 + 50)/50 \quad (9)$$

where $n_{corrected}$ is the corrected particle number, n_{raw} is the detected particle count, ln is the natural log, and d is the representative diameter of the grain-size class. This sediment-count-correction is not required for estimating the impact of bedload on attached-algae removal because the actual number of sediment impacts is essential for the removal of attached-algae.

Overestimation of smaller diameters due to multiple impacts can be accounted for using two steps. The first step entails accounting for the number of excess counts based on:

$$n_{excess} = n_{corrected}(\max(0, 28.209\ln(d) - 30.81 - [-16.41\ln(d) + 55.052] - 50)/50) \quad (10)$$

where n_{excess} indicates the estimated number of excess counting occurrences. The trend in underestimations of grain size was analyzed in Figure 10. The ratio of 0.39 for mass, as shown in Figure 10, corresponds to a ratio of $0.39^{1/3} = 0.703$ for diameter and roughly corresponds to one class smaller for diameter class. Accordingly, n_{excess} for each grain-size class, d_{gi}, is calculated and the sediment count of one class smaller, d_{gi-1}, is subtracted by n_{excess} estimated from $n_{corrected}$ from d_{gi}.

4. Site Location and Target Events

4.1. Overview of the River

Our study was conducted in a river reach of the Jyoge River, a tributary of the Gouno River system. The river course is regulated by bank protection and the bank to bank width is 40–160 m. The average slope is 0.0032. The Haizuka Dam was installed within the Jyoge River and has been operating since 2006. The river reach surveyed for our study is a 10 km section located downstream from the dam. Figure 12 provides a map of the surveyed reach and measuring points. Measurement devices were placed on the river bed at

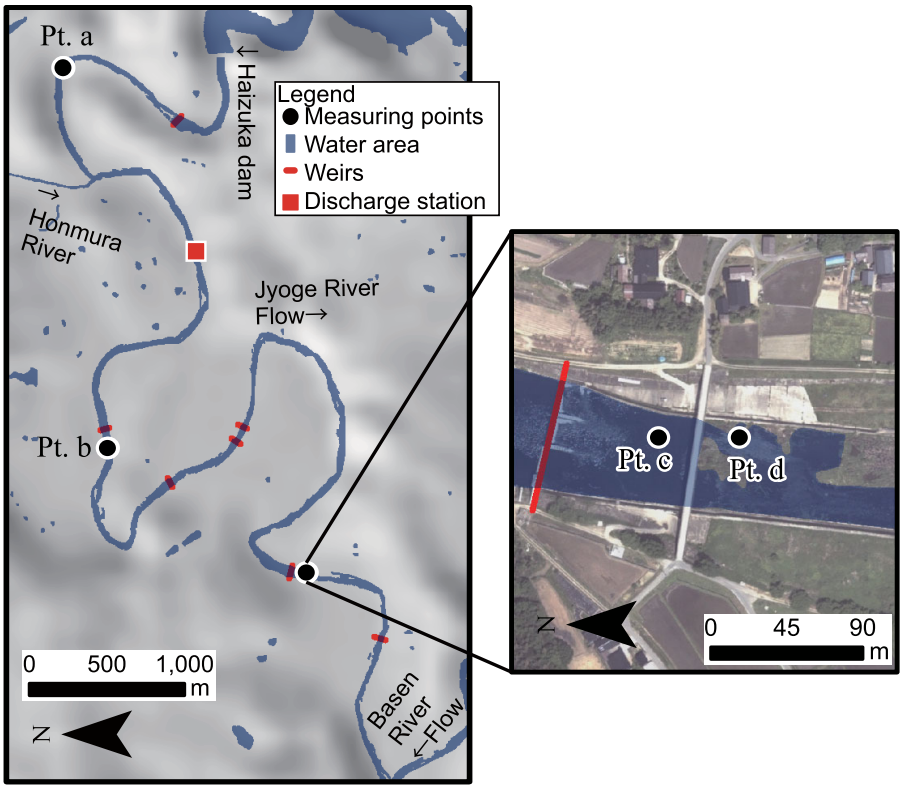

Figure 12. The field site and measuring stations within the Jyoge River, Hiroshima, Japan.

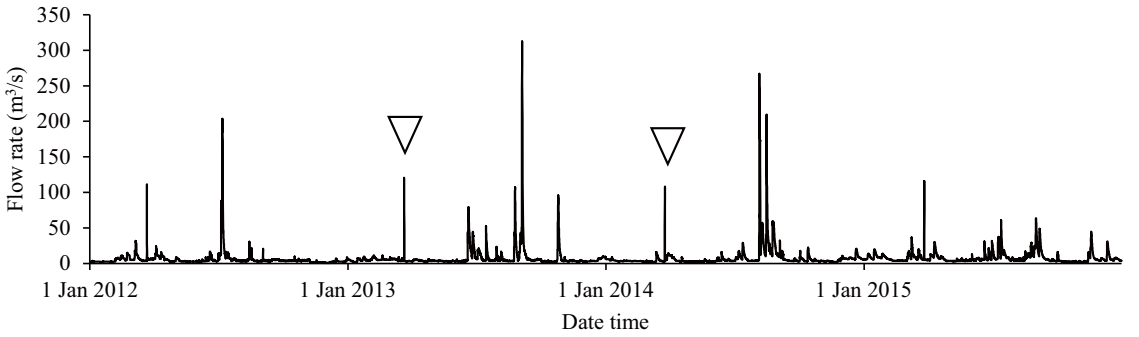

Figure 13. A discharge hydrograph at the discharge station. The two triangles indicate the two flushing flows events we focused on for this study.

the measuring points during the dam's flushing flows. Chl-a density relative to biomass attached to cobbles at Pts. a, b, and d prior to and following the flushing flow conducted in 2012 was measured. Pt. c was located within an *Egeria-densa* patch and the biomass change of aquatic plants surrounding Pt. c prior to and following the flushing flow conducted in 2013 was also surveyed.

4.2. Flushing Flow Events

At the field site used for our study, flushing flows have been conducted every spring and mimic the snowmelt floods that naturally occurred prior to dam construction. No sediment bypassing facility is located at the dam. Flushing flows have been used to release water from the dam, but sediment discharging has not been a part of this process. Figure 13 provides a discharge hydrograph for the discharge station, depicted as a filled square in Figure 12. Discharge was calculated based on water level data using rating curves calibrated by the river authority. Figure 14 provides a close-up of hydrographs for the two flushing flow events we focused on for this study. As compared to the 21 March 2013 event, the flushing flow conducted on 25 March 2014 (located on the right in Figure 14) consisted of a shorter duration for the descending phase of the flow rate in order to reduce the total amount of water released from the dam.

4.3. Flow and Bed Material at the Measuring Points

Table 3 summarizes bulk flow properties for the peak flow rate ($Q = 100$ m^3/s) during the 2013 and 2014 flushing flows. Sixty percent, 50%, and 84% of the finer grain size of the top layer at each of the measuring points are also provided in Table 3. To measure the grain size distribution, 100 grains were sampled at an equal distance within the grid for the top layer, and the arithmetic mean of the major, intermediate, and minor axis lengths was used as the grain size [*García*, 2008]. An aquatic plant patch covered the bed at Pt. c and the bed surface was covered by silt and sand [*Jones et al*., 2012]. Therefore, we were not able to sample in this area without disturbance. The bed shear stresses of flow cases Q30 and Q20 (the calibration experiment reported in section 3) were 36 and 31 Pa, respectively, and corresponded to the bed shear stress at Pt. d during peak water levels.

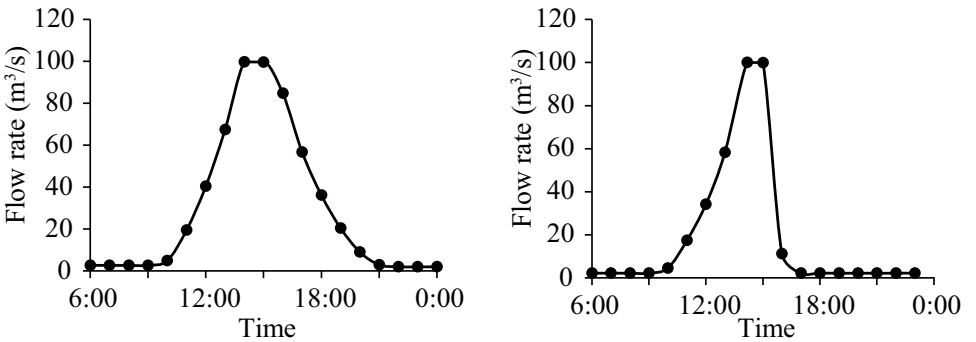

Figure 14. Discharge hydrographs for two flushing flows; (left): 21 March 2013; (right): 25 March 2014.

Table 3. Bulk Channel Geometry, Bulk Flow Properties During the Peak Flow Rate, and the Grain-Size of the Top Layer

Point Name	Width B (m)	Slope I (−)	Top Layer Bed-Material D_{16} (mm)	D_{50} (mm)	D_{84} (mm)	Water Depth H (m)	Bed Shear Stress τ_0 (Pa)
Pt. a	39.8	0.0027	46	69	95	1.7	46
Pt. b	49.4	0.0079	65	136	260	1.5	116
Pt. c	47.9	0.0024	(Silt and Sand Under Aquatic Plant Cover)			2.6	61
Pt. d	47.9	0.0024	42	71	106	1.4	33

5. Results and Discussion

5.1. The Flushing Flow During March 2013

The 44.1 kHz measuring device was installed in the river bed at Pts. a, b, and d. Figure 15 displays estimated impact counts for the four size classes, summarized at 1 h intervals following correction of the grain-size distribution and multiple impact errors. The time-series for the local water level at each point is also provided. The results indicate that the majority of transported gravel had a diameter smaller than 10 mm. Sediment transport was relatively active during the rising phase at Pt. a. No sediment impact was detected at Pt. b. Sediment transport at Pt. d had a profile similar to that of the water level hydrograph but the phase was roughly delayed by 1 h.

Figure 16 displays the change in chl-a density for biomass attached to cobbles at Pts. a, b, and d. The chl-a density at Pts. a and d was reduced by 20% and 37%, respectively, following the flushing flow; whereas the quantity of chl-a at Pt. b was not reduced, based on the mean, following flushing flow implementation.

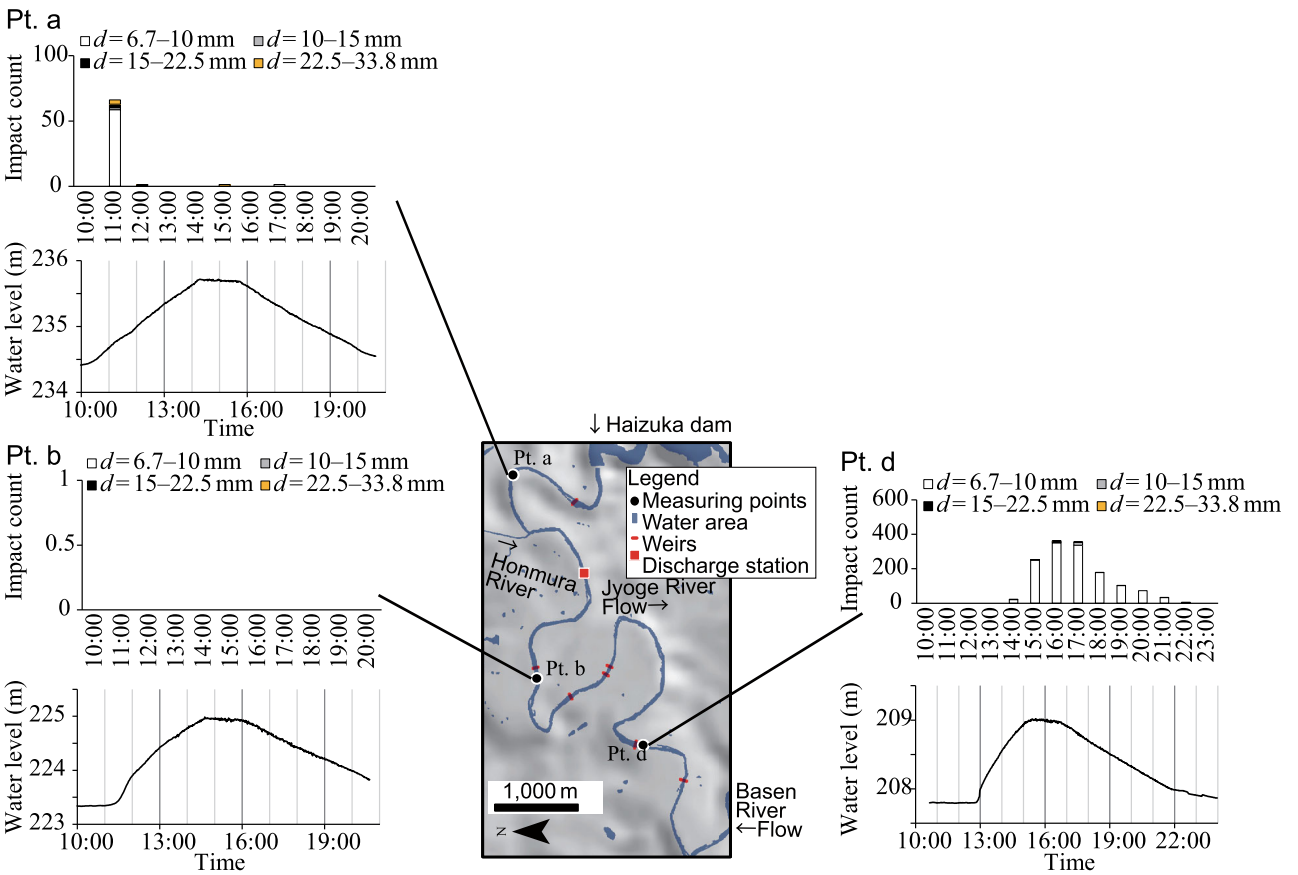

Figure 15. The time-series change of sediment impact counts and the water level at Pts. a, b, and d during the 2013 flushing flow. Impact counts were separated into three diameter size classes.

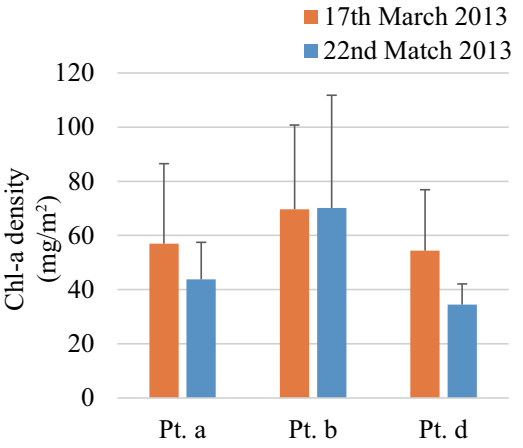

Figure 16. The chl-a density at Pts. a, b, and d prior to and following the 2013 flushing flow. The mean (bar length) and the standard deviation (error bar) were calculated based on three samples obtained at each point.

5.2. The Flushing Flow During March 2014

Results obtained from four devices embedded in the river during the 2014 flushing flow are provided in Figure 17. The locations where devices were placed at Pts a, b, and d in March 2014 were almost identical (within 5 m) to the areas measured in March 2013. Sediment transport at Pts. a and d displayed profiles similar to local water level change. Impact counts at Pts. b and c were only four and one, respectively. Pt. c was located within a patch of macrophytes.

The change in dry biomass for aquatic plant cover at Pt. c is summarized in Figure 18. Aquatic plant biomass was reduced 38% following flushing flow. The aquatic plant species *Egeria densa* settled in this area. *Egeria densa* originated from South America and is inactive during the winter to early spring in the region surveyed, so growth between flushing

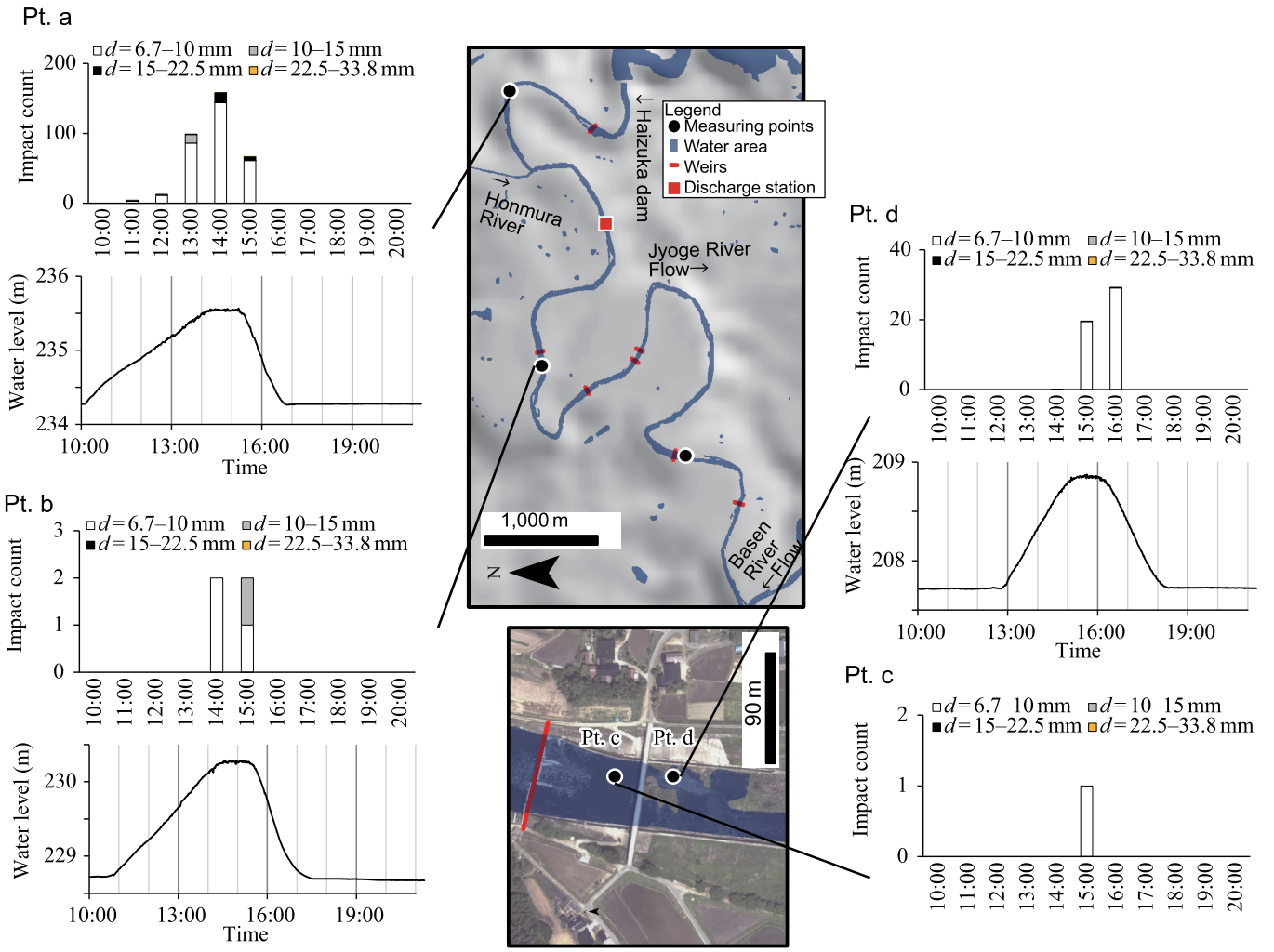

Figure 17. The time-series change of sediment impact counts and water levels at Pts. a to d during the 2014 flushing flow.

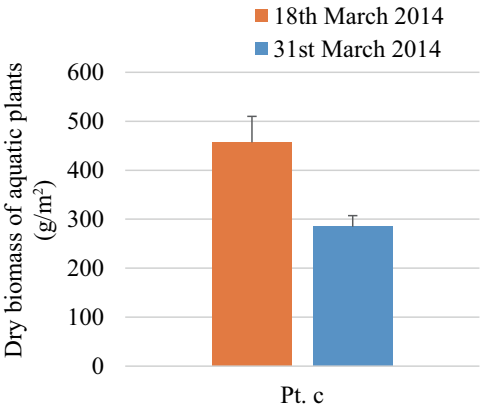

Figure 18. Dry biomass of aquatic plants at Pt. c. The mean (bar length) and the standard deviation (error bar) were calculated based on four samples.

flow implementation (25 March 2014) and biomass sampling (31 March 2014) can be considered to be negligible.

5.3. Discussion

5.3.1. Gravel Transport Impact on the Reduction of Attached-Algae and Aquatic Plants

Chlorophyll-a density at Pts. a and d was substantially reduced following flushing flows, whereas chl-a density at Pt. b was practically unchanged (Figure 16). The result indicates that some amount of gravel transport was detected at Pts. a and d, but none was recorded at Pt. b (Figure 15). Thus, the hypothesis that gravel saltation contributes to the remove of attached-algae [*Tsujimoto and Tashiro*, 2004; *Fovet et al.*, 2010] was supported by our results.

Aquatic plant biomass at Pt. c was substantially reduced following the 2014 flushing flow. The measurement device placed in the aquatic plant patch at Pt. c detected almost negligible gravel impact (only four impacts were detected throughout the event). The result implies that the reduction of aquatic plant biomass at Pt. c during the flushing flow was not related to the transport of sediment with diameters larger than 6.7 mm. Due to small kinetic momentum, smaller sediment particles are expected to have limited the contribution and efficiency for the abrasion of aquatic plant bodies. The reduction of aquatic plant biomass may be due not to sediment impact but to a fluid force acting on plant bodies.

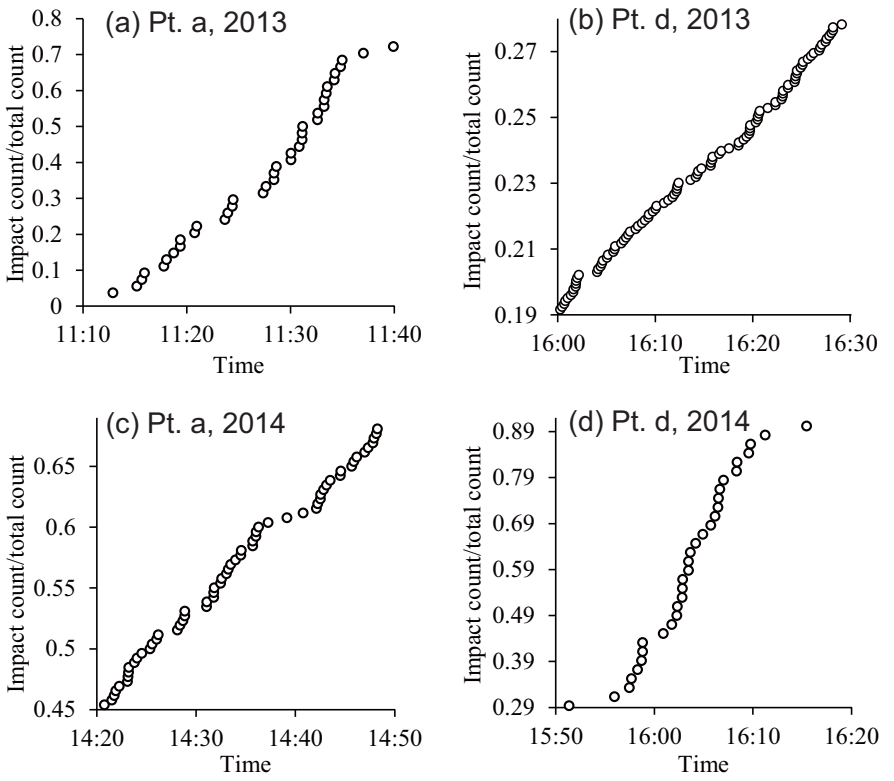

Figure 19. The time-series increase of impact counts at Pts. a and d during the March 2013 and March 2014 flushing flows.

5.3.2. The Gravel Transport Process

Based on our measurements, amounts of gravel bedload were limited. Gravel ($2 < d < 32$ mm) was quite rare in the top layer (see D_{16} in Table 3). The result suggests that gravel transport during flushing flows was supply-limited partial sediment transport [*Kleinhans et al*., 2002; *Kuhnle et al*., 2006; *Tuijnder et al*., 2009]. In regards to fine sediment transport on an immobile coarse sediment layer, fine sediment forms structured bed-forms such as sand-ribbons or dunes and the form of the bed is regulated not only by flow power but by finer fraction supply from the upstream [*Kleinhans et al*., 2002; *Tuijnder et al*., 2009].

To investigate the existence of structured bedload transport, we created time-series plots of impact count increases at Pts. a and d for March 2013 and March 2014, as depicted in Figure 19. In these plots, the steep-sloped area corresponds to the interval when gravel transport was active, and flat and spare regions indicate periods when gravel transport was inactive. Periodic switching of steep and flat slopes is found in Figure 19. The duration of this switching had an order of 2–15 min. The interval is substantially large as compared to the time-scale for ejection/sweep events (an order of 1 s) [*Drake et al*., 1988; *Shvidchenko and Pender*, 2001] and kolk/boil structures (an order of 30 s) [*Jackson*, 1976; *Babakaiff and Hickin*, 1996; *Best*, 2005].

Kuhnle et al. [2006] reported bed-form migration in Goodwin Creek where the median bed material size was 22.6 mm for the large fraction and 0.4 mm for the fine fraction. The mean bed shear stress was in the range of 2.5–24.8 Pa. The time duration of bed-form passing (the bed-form period) was 6.3–53 min. The ratio between the bed-form length and the bed-form period was 0.24–0.54 m/min. Assuming that this ratio is applicable to our site, owing to the similarity in flow conditions, the estimated bed-form length is 1.2–2.7 m for our site based on a bed-form period of 5 min. The amount of detected gravel impact per bed-form period (5 min) was quite limited in regard to bed-form dimensions. The result suggests that the bed-form consisted not only of detected gravel but also of sand not measured by our devices. Grains finer than 6.7 mm could not be directly measured by the device but are expected to migrate with coarser detectable grains during flushing flows, to comprise migrating bed-forms, and to contribute to the removal of biofilm from cobbles. At Pt. b, the transport of finer grains was not present or limited. Finer grains appeared to move with larger gravel that was detectable, so the lack of gravel detection at Pt. b may indicate that the transport of finer grains was also quite limited and that this limited transport of grains included limited transport for the finer fraction, causing the chl-a density to be constant during flushing flows.

6. Conclusions

In this work, we presented a new geophone-based method for detecting non-uniform gravel bedload in cobble-bed rivers. The device presented is small and can be installed by hand in a river bed. The geophone device was designed to measure partial bedload transport on a river bed undisturbed by device installation. To accomplish this purpose, we designed the device to mimic the size and shape of bed-material. The relationship between acoustic waveforms and sediment diameters was evaluated using a flume experiment. A number of proposed devices were then used for observing gravel transport during flushing flows implemented during March 2013 and 2014. The size and amount of bedload transport occurring during flushing flows was successfully estimated and relationships related to the removal of attached-algae and aquatic plants were discussed.

The developed device consists of inexpensive consumer products, including a sound recorder. Therefore, distributing a great number of devices at an affordable cost is possible. In the future, we will investigate gravel transport by combining a number of devices and pressure sensors so we can analyze the interaction between bedload transport and near bed flow turbulence in actual rivers during floods.

At present, due to digital recorder control limitations and memory capacity, sequential bedload measurements are limited to approximately 5 days following bed installation. For applications during natural floods, a longer standby time ($>$1 month) is required. Additionally, the accuracy of mass and velocity estimates for sediment, as well as the device's ability to detect smaller particles, should be improved in order to obtain a more detailed understanding of gravel transport in cobble-bed rivers.

Appendix A

The mean and standard deviation for each experimental case discussed in section 3.3. and plotted in Figure 9 are summarized quantitatively in Table A1.

Table A1. The Mean and Standard Deviation for Each Experimental Case

Recorder	96 kHz Recorder									
Flow case	Q20			Q30			Q30			
Size class	S12	S20	S30	S12	S20	S30	G08	G13	G20	G28
Actual mean mass (g)	2.5	9.9	35.5	2.5	9.9	35.5	1.1	2.4	5.7	16.1
Mean of estimated mass (g)	4.3	7.1	39.4	4.0	7.9	15.4	1.1	2.2	4.0	10.3
Standard deviation of estimated mass (g)	4.3	5.4	34.5	7.3	6.5	15.1	1.4	2.0	3.3	9.3
Recorder	44.1 kHz recorder									
Flow case	Q20			Q30			Q30			
Size class	S12	S20	S30	S12	S20	S30	G08	G13	G20	G28
Actual mean mass (g)	2.5	9.9	35.5	2.5	9.9	35.5	0.9	2.2	7.3	15.7
Mean of estimated mass (g)	2.6	10.9	33.7	2.2	12.6	36.9	N.D.	1.4	5.6	13.6
Standard deviation of estimated mass (g)	1.7	4.9	30.5	2.4	6.3	17.7		1.5	4.4	13.0

Acknowledgments
We thank the Miyoshi office of the River and National Highway office of Miyoshi and the administration office of Haizuka Dam and the Chugoku Regional Development Bureau for providing fundamental data regarding flushing flows and the Jyoge River. Our work was supported by: a grant from the Furukawa foundation; Grant-in-Aid of Japan Society for the Promotion of Science (JSPS) (B), 23360215; the River Fund in charge of the Foundation of River and Watershed Environment Management (FOREM) Japan, 251212009; Grant-in-Aid for Young Scientists (B), 26820205; the National Natural Science Foundation of China, 51379137 and 51579162; the Open Fund of the State Key Laboratory of Hydraulics and Mountain River Engineering at Sichuan University, SKHL1301; and Grant-in-Aid of Japan Society for the Promotion of Science (JSPS) (C), 16K06609. The collected and processed field/laboratory data are available from the corresponding author.

References

Babakaiff, C. S., and E. J. Hickin (1996), Coherent flow structures in Squamish River Estuary, British Columbia, Canada, in *Coherent Flow Structures in Open Channels*, edited by P. J. Ashworth et al., pp. 321–342, John Wiley, Hoboken, N. J.

Best, J. (2005), The fluid dynamics of river dunes: A review and some future research directions, *J. Geophys. Res.*, *110*, F04S02, doi:10.1029/2004JF000218.

Chung, C. C., and C. P. Lin (2011), High concentration suspended sediment measurements using time domain reflectometry, *J. Hydrol.*, *401*(1), 134–144.

Clayton, J. A., and J. Pitlick, J. (2007), Spatial and temporal variations in bed load transport intensity in a gravel bed river bend, *Water Resour. Res.*, *43*, W02426, doi:10.1029/2006WR005253.

Clifford, N. J., A. Robert, and K. S. Richards (1992), Estimation of flow resistance in gravel–bedded rivers: A physical explanation of the multiplier of roughness length, *Earth Surf. Processes Landforms*, *17*(2), 111–126.

Diplas, P., R. Kuhnle, J. Gray, D. Glysson, and T. Edwards (2008), Sediment transport measurements. Sedimentation engineering: Processes management, modeling, and practice, in *ASCE Manuals and Reports on Engineering Practice*, edited by M. H. García, no. 110, pp. 307–354, ASCE, Reston, Va.

Drake, T. G., R. L. Shreve, W. E. Dietrich, P. J. Whiting and L. B. Leopold (1988), Bedload transport of fine gravel observed by motion-picture photography, *J. Fluid Mech.*, *192*, 193–217.

Feijoó, C. S., F. R. Momo, C. A. Bonetto, and N. M. Tur (1996), Factors influencing biomass and nutrient content of the submersed macrophyte *Egeria densa* Planch. in a pampasic stream. *Hydrobiologia*, *341*(1), 21–26.

Fovet, O., G. Belaud, X. Litrico, S. Charpentier, C. Bertrand, A. Dauta, and C. Hugodot (2010), Modelling periphyton in irrigation canals, *Ecol. Modell.*, *221*(8), 1153–1161.

Fovet, O., G. Belaud, X. Litrico, S. Charpentier, C. Bertrand, P. Dollet and C. Hugodot (2012), A model for fixed algae management in open channels using flushing flows, *River Res. Appl.*, 28(7), 960–972.

García, M. H. (2008), Sediment transport and morphodynamics. Sedimentation engineering: Processes management, modeling, and practice, in *ASCE Manuals and Reports on Engineering Practice*, edited by M. H. García, no. 110, pp. 307–354, ASCE, Reston, Va.

Gibson, S., D. Abraham, R. Heath, and D. Schoellhamer (2009), Vertical gradational variability of fines deposited in a gravel framework, *Sedimentology*, *56*(3), 661–676.

Goto, K., T. Itoh, T. Nagayama, M. Kasai, and T. Marutani (2014). Experimental and theoretical tools for estimating bedload transport using a Japanese pipe hydrophone, *Int. J. Erosion Control Eng.*, *7*(4), 101–110.

Hasegawa, Y., and K. Miyamoto (2014), Experimental study natural resonance modes of sound of a hydrophone and sediment discharge measurement [in Japanese with English abstract], *J. Jpn. Soc. Erosion Control Eng.*, *66*(5), 23–32, doi:10.11475/sabo.66.5_23.

Horner, R. R., E. B. Welch, M. R. Seeley, and J. M. Jacoby (1990), Responses of periphyton to changes in current velocity, suspended sediment and phosphorus concentration, *Freshwater Biol.*, *24*(2), 215–232.

Igarashi, T., M. Goto, and A. Kawasaki (1984), Study on impact sound: 1st Report, collision of ball against plate [in Japanese], *Trans. Jpn. Soc. Mech. Eng. Ser. C*, *50*(453), 840–847.

Jackson, R. G. (1976), Sedimentological and fluid–dynamic implications of the turbulent bursting phenomenon in geophysical flows, *J. Fluid Mech.*, *77*(3), 531–560.

Jones, J. I., A. L. Collins, P. S. Naden, and D. A. Sear (2012), The relationship between fine sediment and macrophytes in rivers, *River Res. Appl.*, *28*(7), 1006–1018.

Kleinhans, M. G., A. W. E. Wilbers, A. De Swaaf, and J. H. Van Den Berg (2002), Sediment supply-limited bedforms in sand-gravel bed rivers, *J. Sediment. Res.*, *72*(5), 629–640.

Kuhnle, R. A., J. K. Horton, S. J. Bennett, and J. L. Best (2006), Bed forms in bimodal sand–gravel sediments: Laboratory and field analysis, *Sedimentology*, *53*(3), 631–654.
Lisle, T. E. (1995), Particle size variations between bed load and bed material in natural gravel bed channels, *Water Resour. Res.*, *31*, 1107–1118.
Love, A. E. H. (1944), *A Treatise on the Mathematical Theory of Elasticity*, Dover, N. Y.
Miura T., A. Kawakita, Y. Iwasa, and K. Tanimizu (1976), Studies on the submerged plant community in Lake Biwa II. Macroinvertebrates as an important supplier of nitrogenous nutrients in a dense macrophytes zone, *Physiol. Ecol. Jpn.*, *17*, 587–591.
Mizuyama T., M. Fujita, and M. Nonaka M. (2003), Measurement of bed load with the use of hydrophones in mountain torrents, in *Erosion and Sediment Transport Measurement in Rivers*, edited by J. Bogen, T. Fergus and D. Walling, pp. 222–227, IAHS Publ., Wallingford, U. K.
Mizuyama, T., A. Oda, A., J. B. Laronne, M. Nonaka, and M. Matsuoka (2010), Laboratory tests of a Japanese pipe geophone for continuous acoustic monitoring of coarse bedload, *US Geol. Surv. Sci. Invest. Rep.*, *5091*, 319–335.
Muste, M., S. Baranya, R. Tsubaki, D. Kim, H. Ho, H. Tsai, H., and D. Law (2016). Acoustic mapping velocimetry, *Water Resour. Res.*, *52*, 4132–4150, doi:10.1002/2015WR018354.
Niño, Y., M. García, and L. Ayala (1994), Gravel saltation: 1. Experiments, *Water Resour. Res.*, *30*, 1907–1914.
Oda, A., Y. Hirano, M. Watanabe, M. Ochiai, and S. Endo (2011), Experimental study on evaluation of grain diameter using contact time when gravel collides with elastic plate [in Japanese with English abstract], *J. Jpn. Soc. Civ. Eng.*, *67*, 4 PI_1165–I_1170, doi:10.2208/jscejhe.67.I_1165.
Papanicolaou, A. N., P. Diplas, C. L. Dancey, and M. Balakrishnan (2001), Surface roughness effects in near-bed turbulence: Implications to sediment entrainment, *J. Eng. Mech.*, *127*, 211–218.
Parker, G. (1991), Selective sorting and abrasion of river gravel. II: Applications, *J. Hydraul. Eng.*, *117*(2), 150–171.
Parker, G. (2008), Transport of gravel and sediment mixtures. Sedimentation engineering: Processes, measurements, modeling, and practice, in *ASCE Manuals and Reports on Engineering Practice*, edited by M. H. García, no. 110, pp.165–252. ASCE, Reston, Va.
Peterson, C. G. (1996), Response of benthic algal communities to natural physical disturbance, in *Algal Ecology: Freshwater Benthic Ecosystems*, edited by R. Jan Stevenson, M. L. Bothwell and R. L. Lowe, pp. 375–401, Academic, San Diego, Calif.
Pitlick, J., and P. Wilcock (2001), Relations between streamflow, sediment transport, and aquatic habitat in regulated rivers, in *Geomorphic Processes Riverine Habitat*, edited by J. M. Dorava, D. R. Montgomery, B. B. Palcsak, and F. A. Fitzpatrick, pp. 185–198, Wiley/AGU, Washington, D. C.
Porra, R. J., W. A. Thompson, and P. E. Kriedemann (1989), Determination of accurate extinction coefficients and simultaneous equations for assaying chlorophylls a and b extracted with four different solvents: Verification of the concentration of chlorophyll standards by atomic absorption spectroscopy, *Biochim. Biophys. Acta-Bioenerg.*, *975*(3), 384–394.
Powell, D. M. (2014), Flow resistance in gravel–bed rivers: Progress in research. *Earth-Sci. Rev.*, *136*, 301–338.
Raven, E. K., S. N. Lane, and R. Ferguson (2010), Using sediment impact sensors to improve the morphological sediment budget approach for estimating bedload transport rates, *Geomorphology*, *119*(1), 125–134.
Reid, S. C., S. N. Lane, J. M. Berney, and J. Holden (2007), The timing and magnitude of coarse sediment transport events within an upland, temperate gravel–bed river, *Geomorphology*, *83*(1), 152–182.
Rickenmann, D., and B. W. McArdell (2007), Continuous measurement of sediment transport in the Erlenbach stream using piezoelectric bedload impact sensors, *Earth Surf. Processes Landforms*, *32*(9), 1362–1378.
Rickenmann, D., J. M. Turowski, B. Fritschi, A. Klaiber, and A. Ludwig (2012), Bedload transport measurements at the Erlenbach stream with geophones and automated basket samplers, *Earth Surf. Processes Landforms*, *37*(9), 1000–1011.
Sekine, M., and H. Kikkawa (1992), Mechanics of saltating grains. II, *J. Hydraul. Eng.*, *118*(4), 536–558.
Shen, H. W., and J. Y. Lu (1983), Development and prediction of bed armoring, *J. Hydraul. Eng.*, *109*(4), 611–629.
Shvidchenko, A. B., and G. Pender (2001), Macroturbulent structure of open-channel flow over gravel beds, *Water Resour. Res.*, *37*, 709–719.
Tsakiris, A. G., A. T. N. Papanicolaou, and T. J. Lauth (2014), Signature of bedload particle transport mode in the acoustic signal of a geophone, *J. Hydraul. Res.*, *52*(2), 185–204.
Tsujimoto, T., and T. Tashiro (2004), Application of population dynamics modeling to habitat evaluation - Growth of some species of attached algae and its detachment by transported sediment, *Hydroécol. Appl.*, *14*, 161–174.
Tuijnder, A. P., J. S. Ribberink, and S. J. Hulscher (2009), An experimental study into the geometry of supply–limited dunes, *Sedimentology*, *56*(6), 1713–1727.
Uchida T., A. Okamoto, S. Hayashi, T. Suzuki, A. Fukumoto, S. Yamashita, and S. Tagata (2013), Hydrophone observations of bedload transport in mountainous rivers of Japan, paper presented at the 12th ISRS Symposium (Advances in River Sediment Research), pp. 1749–1756, World Association for Sedimentation and Erosion Research (WASER) and International Research and Training Center on Erosion and Sedimentation (IRTCES), Kyoto, Japan.
Vericat, D., M. W. Smith, and J. Brasington (2014), Patterns of topographic change in sub-humid badlands determined by high resolution multi-temporal topographic surveys, *Catena*, *120*, 164–176.
Wolfert, H. P., A. J. M. Koomen, and G. J. Maas (2001), Geomorphological Change and River Rehabilitation, Case studies on lowland fluvial systems in the Netherlands, Alterra Scientific Contributions 6, PhD thesis of Utrecht University, pp. 33–58, Alterra green world research, Wageningen, the Netherlands.
Yager, E. M., J. W. Kirchner, and W. E. Dietrich (2007), Calculating bed load transport in steep boulder bed channels, *Water Resour. Res.*, *43*, W07418, doi:10.1029/2006WR005432.
Yeh, W. W. G. (1986), Review of parameter identification procedures in groundwater hydrology: The inverse problem, *Water Resour. Res.*, *22*, 95–108.
Zener, C. (1941), The intrinsic inelasticity of large plates, *Phys. Rev.*, *59*(8), 669.